Interlayer vibrational modes in few-quintuple-layer Bi_2Te_3 and Bi_2Se_3 two-dimensional crystals: Raman spectroscopy and first-principles studies

Yanyuan Zhao,[1,*] Xin Luo,[2,5,*] Jun Zhang,[1] Junxiong Wu,[3] Xuxu Bai,[4] Meixiao Wang,[4] Jinfeng Jia,[4] Hailin Peng,[3] Zhongfan Liu,[3] Su Ying Quek,[2,5,†] and Qihua Xiong[1,6,†]

[1]*Division of Physics and Applied Physics, School of Physical and Mathematical Sciences, Nanyang Technological University, Singapore 637371, Singapore*

[2]*Institute of High Performance Computing, 1 Fusionopolis Way, #16-16 Connexis, Singapore 138632, Singapore*

[3]*Center for Nanochemistry, Beijing National Laboratory for Molecular Sciences (BNLMS), College of Chemistry and Molecular Engineering, Peking University, Beijing 100871, People's Republic of China*

[4]*Department of Physics, Key Laboratory of Artificial Structures and Quantum Control, Ministry of Education, Shanghai Jiao Tong University, Shanghai 200240, People's Republic of China*

[5]*Department of Physics, Centre for Advanced 2D Materials and Graphene Research Centre, National University of Singapore, 6 Science Drive 2, Singapore 117546, Singapore*

[6]*NOVITAS, Nanoelectronics Centre of Excellence, School of Electrical and Electronic Engineering, Nanyang Technological University, Singapore 639798, Singapore*

(Received 20 September 2014; revised manuscript received 19 November 2014; published 23 December 2014)

Layered materials, such as graphite/graphene, boron nitride, transition metal dichalcogenides, represent materials in which reduced size, dimensionality, and symmetry play critical roles in their physical properties. Here, we report on a comprehensive investigation of the phonon properties in the topological insulator Bi_2Te_3 and Bi_2Se_3 two-dimensional (2D) crystals, with the combination of Raman spectroscopy, first-principles calculations, and group theory analysis. Low frequency ($<30\,cm^{-1}$) interlayer vibrational modes are revealed in few-quintuple-layer (QL) Bi_2Te_3/Bi_2Se_3 2D crystals, which are absent in the bulk crystal as a result of different symmetries. The experimentally observed interlayer shear and breathing mode frequencies both show blueshifts, with decreasing thickness in few-QL Bi_2Te_3 (down to 2QL) and Bi_2Se_3 (down to 1QL), in agreement with first-principles calculations and a linear chain model, from which the interlayer coupling force constants can be estimated. Besides, an intense ultralow ($<12\,cm^{-1}$) frequency peak is observed in 2–4QL Bi_2Te_3, which is tentatively attributed to a substrate-induced interface mode supported by a linear chain model analysis. The high frequency Raman peaks exhibit frequency shifts and broadening from 3D to 2D as a result of the phonon confinement effect. Our studies shed light on a general understanding of the influence of dimensionality and crystal symmetry on the phonon properties in layered materials.

DOI: 10.1103/PhysRevB.90.245428 PACS number(s): 63.22.Np, 78.66.Hf, 31.15.A−

I. INTRODUCTION

Two-dimensional (2D) crystals represent those atomic scale crystalline layers that function as the building blocks for a variety of layered materials, including graphite, boron nitride, a large family of transition metal dichalcogenides, some transition metal oxides and iodides, and some group III, IV, and V metal chalcogenides [1,2]. Compared to their bulk counterparts, the properties of 2D crystals can be readily tuned, owing to their unique dimensionality and structural anisotropy, where heat and charge transport are highly confined. The V–VI compounds (Bi_2Te_3, Bi_2Se_3 and Sb_2Te_3) are among the most extensively studied layered materials for their historically well-known thermoelectric properties [3], as well as their recently discovered properties as topological insulators [4]. Nanostructured Bi_2Te_3 and Bi_2Se_3, especially in 2D geometry, are favorable for the investigation of the topological insulating properties due to the large surface-to-volume ratio and have been extensively studied through electron transport measurements [5–8]. Considerable improvement on the thermoelectric performance has also been achieved in the Bi_2Te_3 and Bi_2Se_3 related nanocomposites due to the increased phonon scatterings by the interfaces and grain boundaries [9–12]. Besides the great progress on the research of their electrical and electronic properties, the phonon properties of Bi_2Te_3 and Bi_2Se_3 and the lattice dynamics, especially in the 2D regime, have also drawn strong interest. From the theoretical point of view, Luo *et al.* [13] and Cheng and Ren [14] compared the phonon properties of Bi_2Te_3/Bi_2Se_3 monolayers and bulk crystals through *ab initio* calculations, from which they believe that the spin-orbit coupling effect is important for determining the phonon frequencies. Experimentally, Raman spectroscopy has been extensively adopted for probing the phonon modes in Bi_2Te_3/Bi_2Se_3 2D crystals. Thickness-dependent Raman spectroscopy in few-quintuple-layer (QL) Bi_2Se_3 (down to 4QL) and Bi_2Te_3 (down to 1QL) have been systematically studied by Zhang *et al.* [15] and Wang *et al.* [16], respectively, in addition to some other scattered reports [17–19].

Dimensionality and symmetry can largely influence the phonon properties in layered materials. From three dimensional (3D) to 2D, due to the change of the crystal symmetry, the intrinsic phonon properties, in terms of phonon mode quantity and optical activity [Raman/infrared (IR) activities], are completely different. In general, more phonon normal modes exist in 2D crystals, and while the Raman active modes

*These authors contributed equally to this work.

†Author to whom correspondence should be addressed: queksy@ihpc.a-star.edu.sg and Qihua@ntu.edu.sg

in bulk are also Raman active in 2D, the reverse is not necessarily true. [20]. Recently, new Raman peaks resulting from a lower symmetry in 2D were reported in few-layer WSe_2 [20]. Moreover, low frequency interlayer vibrational modes have been revealed by Raman spectroscopy in few-layer graphene, MoS_2 and WSe_2 [21–24]. While the in-plane shear modes are also Raman active in bulk, the out-of-plane breathing modes correspond to an optically inactive mode in the bulk crystal [21–23]. The behavior of the interlayer vibrational modes can be well explained by the lowered crystal symmetries in 2D, and were proposed to be universal in all layered materials. However, this has not yet been reported in the topological insulator systems (Bi_2Te_3, Bi_2Se_3, and Sb_2Te_3), despite the extensive Raman reports mentioned above.

Here, we demonstrate the existence of the interlayer vibrational modes in Bi_2Te_3 and Bi_2Se_3 2D crystals in the ultralow frequency region (5–30 cm^{-1}), combining Raman spectroscopy, first-principles calculations and group theory analysis. The low frequency interlayer vibrational modes are strictly excluded in the 3D bulk, due to a higher crystal symmetry. Both the experimentally observed interlayer shear and breathing modes exhibit blueshifts with decreasing thickness, agreeing well with the density functional theory (DFT) calculations, and can be interpreted by a simple linear chain model. Besides, a substrate-induced low frequency phonon mode has been identified in few-layer Bi_2Te_3, which is tentatively believed to arise from the interactions between the Bi_2Te_3 thin films and the substrates. In the high frequency regime, Raman peaks corresponding to the bulk phonon normal modes are found to exhibit variations in frequency and linewidth in 2D crystals, which can be well understood by the phonon confinement effect.

II. METHODS

A. Sample preparation

Bi_2X_3 (X = Se, Te) nanoplates were synthesized through a vapor transport growth in a horizontal tube furnace (Lindberg/Blue M) equipped with a quartz tube [25,26]. During the growth, Bi_2X_3 power (99.99%, Alfa Aesar) was positioned in the center of the quartz tube as the source material, while commercial 100 nm SiO_2/Si substrates precleaned by isopropyl alcohol or freshly cleaved fluorophlogopite mica substrates were placed downstream from the powder source. The growth chamber was first evacuated to ∼5 mTorr and then flushed several times with the argon carrier gas. Typical growth of Bi_2Se_3 nanoplates was conducted at ∼500 °C with a 30–50 sccm gas flow rate and 100 Torr pressure for 5–10 min. The growth conditions for B_2Te_3 nanoplates were generally similar to the Bi_2Se_3 case but at a lower temperature of ∼480 °C. The as-grown samples were stored in electronic dry cabinets (Digi-Cabi) with the relative humidity maintained around 25%. Raman measurements were performed on Bi_2X_3 nanoplates within a few days after growth.

B. Raman spectroscopy

Raman scattering spectroscopy measurements were carried out at room temperature using a micro-Raman spectrometer (Horiba-JY T64000) equipped with a liquid nitrogen cooled charge-coupled device. The measurements were conducted in a backscattering configuration excited with a helium-neon laser ($\lambda = 632.8$ nm). The laser sidebands are effectively filtered out with the adoption of a reflecting Bragg grating (OptiCrate) followed by another ruled reflecting grating, thus a detection limit of ∼5 cm^{-1} can be achieved. The backscattered signal was collected through a 100× objective and dispersed by a 1800 g/mm grating under a triple subtractive mode with a spectra resolution of 1 cm^{-1}. The laser power was kept below 0.05 mW to avoid sample damage and any heating effect.

C. Calculation details

First-principles calculations of vibrational Raman spectra are performed within DFT as implemented in the plane-wave pseudopotential code Quantum ESPRESSO [27]. The local density approximation (LDA) [28] to the exchange-correlation functional is employed in the norm-conserving [29] pseudopotential throughout the calculation. Spin-orbit coupling effects are included self-consistently by using fully relativistic pseudopotentials for the valence electrons. Raman intensities are calculated with density functional perturbation theory (DFPT). To obtain converged results, plane-wave kinetic energy cutoffs of 50 and 500 Ry are used for the wave functions and charge density, respectively. The slabs are separated by 16 Å of vacuum to prevent interactions between slabs (this value has been tested for the convergence of phonon frequencies). Monkhorst-Pack k-point meshes of 13×13×13 and 13×13×1 are used to sample the Brillouin zones for the bulk and thin film systems, respectively. In the self-consistent calculation, the convergence threshold for energy is set to 10^{-9} eV. All the atomic coordinates and lattice constants are optimized with the Broyden-Fletcher-Goldfarb-Shanno quasi-Newton algorithm. During the structure optimization, the symmetry of hexagonal is imposed on NQL (N is the number of QLs). The structures are considered as relaxed when the maximum component of the Hellmann-Feynman force acting on each ion is less than 0.003 eV/Å.

To estimate the effect of the substrate on the linear chain model, we add a substrate force constant K_i to the self-interaction term of the QL adjacent with the substrate. The self-interaction terms are defined as the diagonal elements of the dynamical matrix, which is constructed with the fitted van der Waals force constants K of first-principles DFT-LDA calculations.

III. RESULTS AND DISCUSSION

Layered Bi_2X_3 (X = Se, Te) is composed of hexagonally close-packed atomic layers arranged along the c axis [30,31]. Each QL consists of five atomic layers covalently bonded to one another with the sequence of X-Bi-X-Bi-X, and has a thickness of around 1 nm. Adjacent QLs are coupled via weak van der Waals interactions and pile up along the c axis infinitely into bulk crystal, crystallizing into a rhombohedral structure [space group $D^5_{3d}(R\bar{3}m)$]. Since the atomic layers are arranged in an /ABC/ stacking manner, the rhombohedral primitive unit cell [black polyhedron in Fig. 1(a)] overruns 3QL and contains five atoms, in accordance with the chemical formula [30,31]. Consequently, there are 15 Brillouin zone center (Γ) phonon modes, 3 acoustic modes, and 12 optical modes. The irreducible representations of the phonon modes

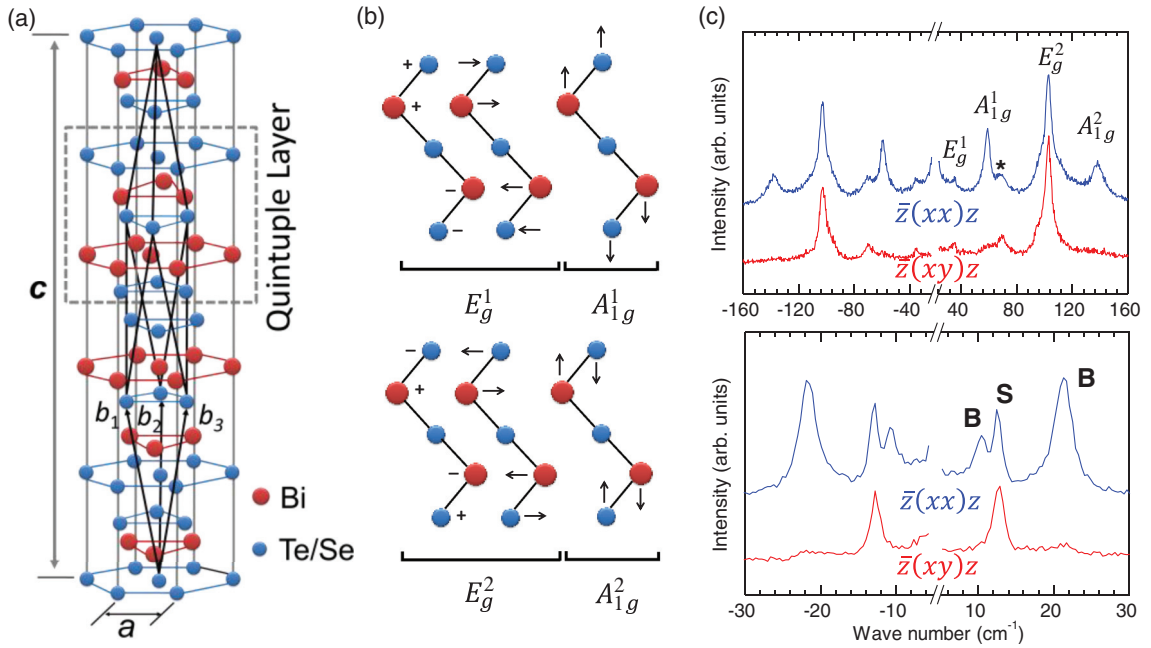

FIG. 1. (Color online) Crystalline structure and Raman modes of Bi_2Te_3. (a) Crystalline structure ($R\bar{3}m$) of Bi_2Te_3/Bi_2Se_3. The primitive unit cell is indicated by the polyhedron (black solid lines). The lattice vectors of the unit cell are shown as the arrows denoted by b_1, b_2, and b_3. (b) Displacement schematics of the Raman active vibrational modes in bulk Bi_2Te_3/Bi_2Se_3. The symbols "+" and "−" stand for vibrating perpendicularly to the paper, inward and outward, respectively. (c) Stokes and anti-Stokes Raman spectra of 3QL Bi_2Te_3 nanoplates on SiO_2/Si substrates under both $z(xx)\bar{z}$ and $z(xy)\bar{z}$ polarization configurations in the high frequency region (top panel, 25–160 cm^{-1}) and low frequency region (bottom panel, 5–30 cm^{-1}).

can be written as $\Gamma_{\text{bulk}} = 3E_u + 3A_{2u} + 2E_g + 2A_{1g}$, among which $2E_g$ and $2A_{1g}$ are Raman active, $2E_u$ and $2A_{2u}$ are IR active, and the rest are acoustic phonon modes (E_u and A_{2u}). The twofold degenerate E symmetry modes represent in-plane (shear) vibrations, while the nondegenerate A symmetry modes vibrate out-of-plane (breathing) along the c axis. The lattice displacements of the Raman active phonon modes in the bulk are displayed in Fig. 1(b), where an equivalent hexagonal unit cell within 1QL is used instead of the complex rhombohedral unit cell for the convenience of demonstration [32].

In Bi_2X_3 2D crystals with finite number of QLs, the crystal symmetry is lowered in comparison to that of its bulk counterpart due to the lack of the translation symmetry along the c axis. Group theory analysis indicates that few-QL Bi_2X_3 has a hexagonal structure that belongs to the space group D_{3d}^3 ($P\bar{3}m1$). The primitive unit cell of an NQL system consists of $5N$ atoms, and the irreducible representations of the zone center phonons can be written as $\Gamma_{\text{odd}} = \frac{5N-1}{2}(A_{1g} + E_g) + \frac{5N+1}{2}(A_{2u} + E_u), N = 1,3,5,\ldots$ for odd-QL systems, while $\Gamma_{\text{even}} = \frac{5N}{2}(A_{1g} + A_{2u} + E_g + E_u), N = 2,4,6,\ldots$ for even-QL systems. Similar to the bulk case, all the E_g and A_{1g} modes are Raman active in few-QL Bi_2X_3, whose Raman tensors have the following forms:

$$A_{1g}: \begin{pmatrix} a & 0 & 0 \\ 0 & a & 0 \\ 0 & 0 & b \end{pmatrix}$$

$$E_g: \begin{pmatrix} c & d & 0 \\ d & -c & 0 \\ 0 & 0 & 0 \end{pmatrix}, \quad \begin{pmatrix} 0 & 0 & d \\ 0 & 0 & c \\ d & c & 0 \end{pmatrix}$$

The Raman intensity of a phonon mode follows the relation $I \propto |e_i \cdot \tilde{R} \cdot e_s|$, where e_i and e_s are the wave vectors of the incident and scattered light and $\tilde{R}$ is the Raman tensor. Our polarized Raman measurements in a backscattering geometry can be described by Porto notations [33], with $\bar{z}(xx)z$ and $\bar{z}(xy)z$ representing the parallel and perpendicular polarization configurations, respectively. Symmetry selection rules predict that both E_g and A_{1g} modes can be observed under the $\bar{z}(xx)z$ configuration, while only the E_g mode is observable under the $\bar{z}(xy)z$ configuration due to its nonzero off-diagonal Raman tensor components [21].

The quantity and behavior of the phonon modes in 2D and 3D Bi_2X_3 can be well understood by the phonon evolution rule: each of the 15 normal modes in 1QL will evolve into N modes in NQL, keeping the vibration manner the same within each QL, while alternating the relative displacement phases among different QLs. The N modes that share the same origin come with very close frequencies, and we call them a *suit* for the convenience of discussion. A suit of modes could have different Raman/IR activities, depending on their vibration symmetries. Following the evolution rule, NQL [space group D_{3d}^3 ($P\bar{3}m1$)] has $15N$ phonon modes (15 suits), and consequently the bulk crystal with infinite QLs should have infinite numbers of phonon modes that, however, are reduced to a finite amount (15) in their irreducible representations due to the higher symmetry [space group D_{3d}^5 ($R\bar{3}m$)]. Following the evolution rule, the in-plane acoustic mode in 1QL will evolve into N-1 interlayer shear modes (E_g and E_u) in NQL, and the out-of-plane acoustic mode evolves into N-1 breathing modes (A_{1g} and A_{2u}), with each QL displacing as a unit and the

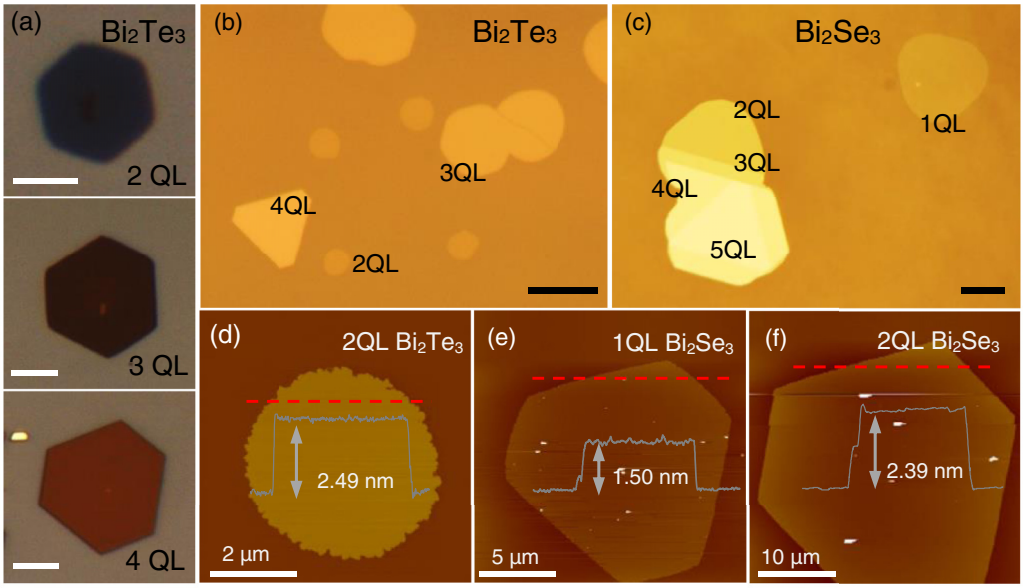

FIG. 2. (Color online) Optical and AFM images of Bi_2Te_3 and Bi_2Se_3 2D crystals grown through a vapor transport method. (a) Optical images of 2–4QL Bi_2Te_3 nanoplates grown on SiO_2/Si substrates. The scale bar is 5 μm. (b) and (c) Optical images of 2–4QL Bi_2Te_3 and 1–5QL Bi_2Se_3 nanoplates grown on mica substrates. The scale bar is 10 μm. (d) and (f) AFM images of 2QL Bi_2Te_3 and 1–2QL Bi_2Se_3 nanoplates on mica. The inset thickness profiles are taken along the red dashed lines.

van der Waals force being the only restoring force. In bulk Bi_2X_3, inter-QL vibrational modes are excluded in the irreducible representations of the Γ phonon modes under its rhombohedral structure. The absence of the interlayer vibrational modes in bulk Bi_2X_3 distinguishes the topological insulator system from other layered materials, such as graphene, MoS_2, and WSe_2, where one of the intrinsic bulk phonon modes corresponds to an interlayer shear mode (E^2_{2g}) [21,24].

In our experiments, Bi_2X_3 2D crystals (down to 2QL for Bi_2Te_3 and down to 1QL for Bi_2Se_3) were synthesized through vapor transport (see Methods) [25,26]. Figures 2(a)–2(c) display the optical images of as-grown 2–4QL Bi_2Te_3 nanoplates on SiO_2/Si and mica substrates and 1–5QL Bi_2Se_3 nanoplates on mica substrates, respectively. The thicknesses of the Bi_2X_3 nanoplates were determined by atomic force microscopy (AFM) measurements, as shown in Figs. 2(d)–2(f), where a thickness of ∼1.5 nm was assigned to 1QL Bi_2X_3 and ∼2.5 nm to 2QL. A slightly larger measured thickness than the predicted value (∼1 nm for 1QL and ∼2 nm for 2QL) is probably due to some adsorbates, such as water molecules, on the surface of the nanoplates, in addition to a surface lattice relaxation effect, where both the inter-QL and intra-QL lattice constants at the surface are expected to increase by a few percent compared to in the bulk [34,35]. Moreover, other factors, such as the force constant difference between the substrates and the nanoplates in the AFM measurements, as well as the substrate-dependent interface spacing [34], might also contribute to the abovementioned discrepancies in the QL number determination based on AFM measured thicknesses. Similarly, the measured thicknesses of the as-grown few-QL Bi_2Te_3 nanoplates on SiO_2/Si also turned out to be larger than the expected values [25]. Despite discrepancies between the theoretical values and the AFM measured results, we believe that our QL number assignment for the Bi_2X_3 nanoplates is correct according to the QL number dependent Raman spectroscopy and first-principles calculations presented in this paper.

Polarized Raman measurements were conducted on as-grown samples, and Fig. 1(c) displays typical Stokes and anti-Stokes Raman spectra of 3QL Bi_2Te_3 on SiO_2/Si substrates under both $\bar{z}(xx)z$ and $\bar{z}(xy)z$ polarization configurations. The top panel shows the high frequency region (30–160 cm^{-1}), where the four intrinsic Raman active phonon modes of bulk (E^1_g, A^1_{1g}, E^2_g and A^2_{1g}) are observed, in accordance with previous observations [36]. The four bulk Raman modes with slightly higher frequencies are also observed in few-QL Bi_2Se_3, with similar results reported by Zhang *et al.* [15] in the polyol synthesized nanoplates. The assignment of the four modes is further verified by their polarization dependence, where the out-of-plane A^1_{1g} and A^2_{1g} peaks are largely suppressed under the $\bar{z}(xy)z$ configuration, while the in-plane E^1_g and E^2_g modes still remain, consistent with the symmetry selection rule. Besides the four Raman active modes, an additional Raman peak located around 69 cm^{-1} (denoted by the black asterisk) was also observed at the higher frequency side of the A^1_{1g} peak under both parallel and perpendicular polarizations, indicating that it corresponds to an in-plane vibrational mode, such as the E^1_g and E^2_g modes. First-principles calculations indicate that this peak is likely to correspond to another mode with E_g symmetry that originates from an IR active E_u mode of 1QL Bi_2Te_3. The calculated frequencies for the E_u suit of modes in few-QL Bi_2Te_3 are around 71 cm^{-1}. In the low frequency range (5–30 cm^{-1}) shown in the bottom panel of Fig. 1(c), three sharp Raman peaks are observed in Bi_2Te_3 with comparable intensities to those of the high frequency peaks. These ultralow frequency Raman features have not been reported yet, to the best of our knowledge. The low frequency characteristics of these peaks

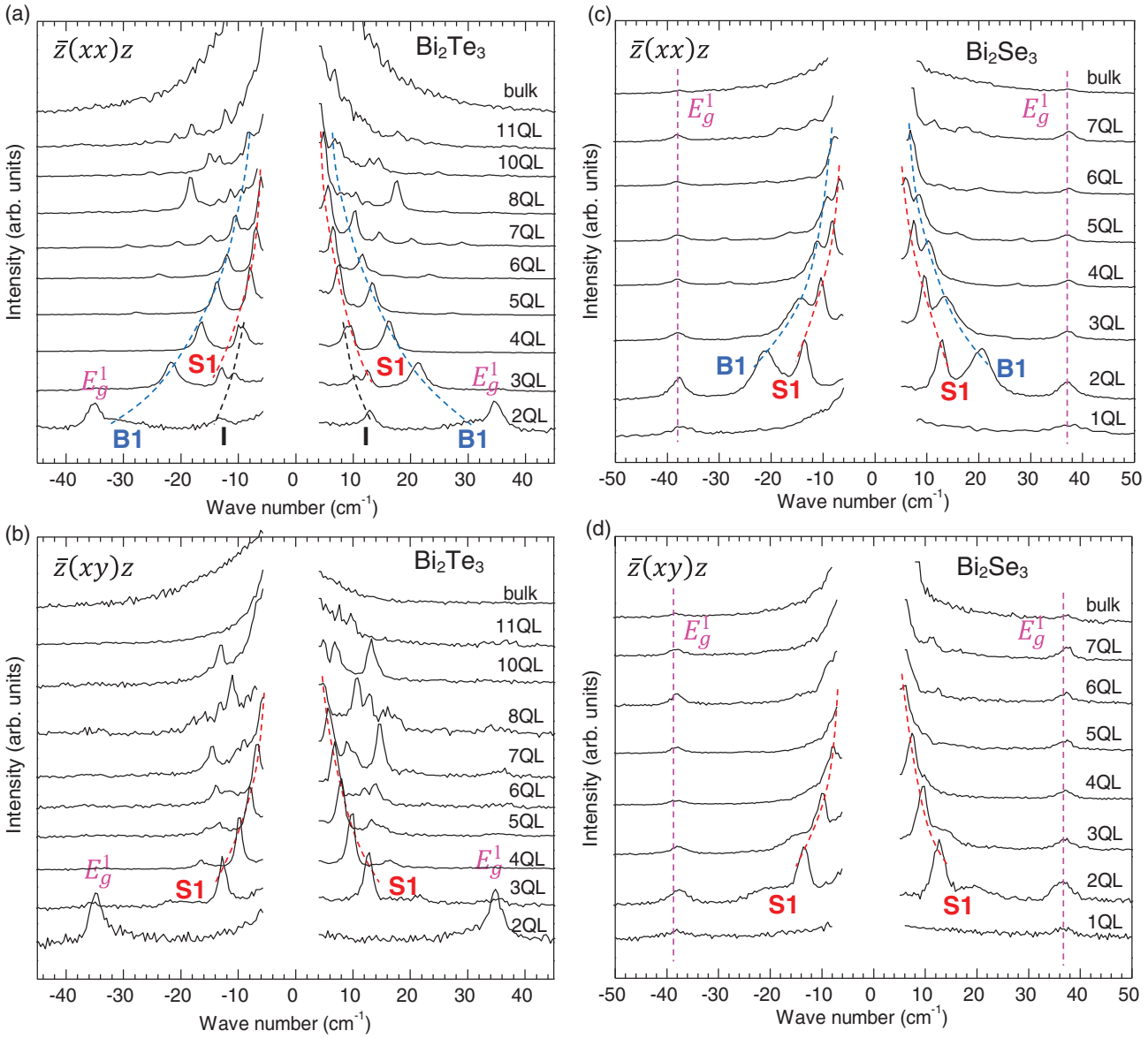

FIG. 3. (Color online) Low frequency Raman spectrum evolutions as a function of QL number in Bi_2Te_3 and Bi_2Se_3. (a) and (b) Low frequency Raman spectra of 2–11QL Bi_2Te_3 on SiO_2/Si substrates measured using the (a) $\bar{z}(xx)z$ polarization configuration, and (b) the $\bar{z}(xy)z$ polarization configurations. (c) and (d) Low frequency Raman spectra of 1–7QL Bi_2Se_3 on mica substrates measured using the (c) $\bar{z}(xx)z$ polarization configuration and (d) the $\bar{z}(xy)z$ polarization configurations. The lowest frequency interlayer breathing, shear modes, and the out-of-plane interface phonon modes are denoted as B1, S1, and I, respectively, and their evolution trends are guided by the red, blue, and black dashed lines.

naturally relate them with the interlayer vibrational modes, as a result of the weak van der Waals restoring force. The polarization dependence of the Raman peaks indicate that two of them likely correspond to the out-of-plane breathing modes (labeled as B), and the other one corresponds to an in-plane shear mode (labeled as S). Note that all the Raman active modes in few-QL and bulk Bi_2X_3 have either E_g or A_{1g} symmetries, the interlayer breathing (B) and shear (S) modes here should correspond to the A_{1g} and E_g vibrational modes, respectively.

To further investigate the ultralow frequency Raman peaks, thickness-dependent Raman measurements were conducted on 2–11QL Bi_2Te_3 on SiO_2/Si substrates, as well as on 1–7QL Bi_2Se_3 on mica substrates. Figure 3 shows the Raman spectrum evolution with varying thickness under both $\bar{z}(xx)z$ Fig. 3(a) and $\bar{z}(xy)z$ Fig. 3(b) polarization configurations. Many low frequency Raman peaks were observed in few-QL Bi_2Te_3 and Bi_2Se_3, whose frequencies are extracted from the spectra and listed in Table S-I and Table S-II (Supplemental Material [37]). Note that the Raman peak located around 35 cm^{-1} in Bi_2Te_3 and 37 cm^{-1} in Bi_2Se_3 corresponds to the E_g^1 mode in the bulk. Among all the Raman features in the low frequency region (5–30 cm^{-1}), two trends of peaks in particular stand out, both showing blueshifts with decreasing thickness, as guided by the blue and red dashed lines. Above 8QL Bi_2Te_3 and 6QL Bi_2Se_3, the two peaks are submerged in the Rayleigh

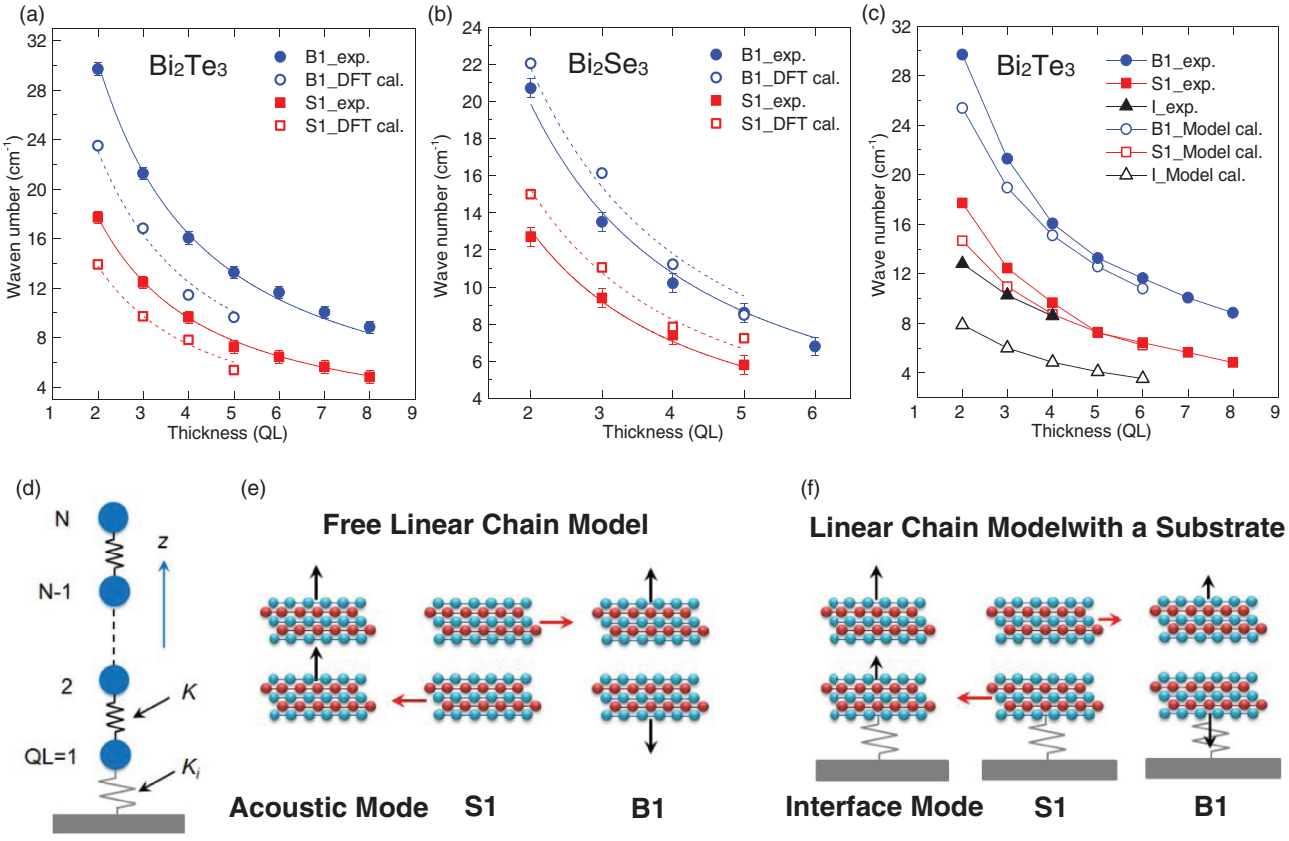

FIG. 4. (Color online) Frequency evolutions of measured and computed interlayer shear, breathing, and interface modes in few-QL Bi_2Te_3 and Bi_2Se_3, as well as and the linear chain model interpretation. (a) and (b) Plot of the lowest frequency shear (S1) and breathing (B1) mode frequencies as a function of QL number in few-QL (a) Bi_2Te_3 and (b) Bi_2Se_3 extracted from Fig. 3. The red solid (dashed) line is the fitting of the experimental (calculated) S1 modes versus thickness using the linear chain model. The blue solid (dashed) line is the fitting for the B1 modes using the same formula as for the S1 modes. (c) Comparison between the experimental and the calculated frequencies for the S1, B1, and I modes through the linear chain model with a substrate with $K_i/K = 0.5$. (d) Schematics of the linear chain model. One blue sphere represents a QL. The force constant is K between nearest-neighbor QLs, and the K_i is the interface force constant between the Bi_2Te_3 nanoplate and the substrates. (e) and (f) Displacement schematics of the I, S1, and B1 modes in 2QL under the (e) free linear chain model and (f) linear chain model with a substrate. The arrows indicate the vibration directions of each QL, and the lengths are proportional to the displacement amplitudes.

scattering background and are beyond the detection limit. DFT calculations indicate that these two peaks correspond to the lowest frequency interlayer breathing (B1) and lowest frequency interlayer shear (S1) modes, respectively, in any NQL system, consistent with their experimental polarization dependence. The frequencies of the B1 and S1 peaks show very high sensitivity to the nanoplate thickness. In Bi_2Te_3, the B1 peak blueshifts by $\sim$21 cm^{-1} from 8QL (8.8 cm^{-1}) to 2QL (30.0 cm^{-1}), and the S1 peak blueshifts by $\sim$13 cm^{-1} from 8QL (4.8 cm^{-1}) to 2QL (18.0 cm^{-1}); in Bi_2Se_3, the B1 peak blueshifts by $\sim$14 cm^{-1} from 6QL (6.8 cm^{-1}) to 2QL (20.7 cm^{-1}), and the S1 peak blueshifts by $\sim$7 cm^{-1} from 5QL (5.8 cm^{-1}) to 2QL (12.7 cm^{-1}). These sensitive frequency evolutions with varying crystal thickness are clearly shown in Figs. 4(a) and 4(b) for Bi_2Te_3 and Bi_2Se_3, respectively. Therefore, low frequency Raman spectroscopy provides a fast and convenient approach to the thickness determination of Bi_2Te_3 and Bi_2Se_3 2D crystals. Note that the B1 and S1 peaks are very weak in 2QL Bi_2Te_3 but still can be identified through a careful Lorentzian fitting and lineshape analysis (see Fig. 5 and Fig. S-1 in the Supplemental Material [37]). In the limit of bulk, no low frequency Raman peaks can be observed at all, in accordance with the group theory analysis that the interlayer vibrational modes do not exist in bulk Bi_2X_3. Raman peaks with frequencies even smaller than that of the S1 peak are identified in 2–4QL Bi_2Te_3, also showing blueshift with decreasing thickness, as guided by the black dashed lines. We tentatively attribute these peaks to an interface mode (labeled as I) resulting from the interactions between the nanoplate and the substrates, which will be discussed later.

First-principles calculations were conducted for the Brillouin zone center phonon frequencies in 1–5QL and bulk Bi_2Te_3/Bi_2Se_3. First principles calculations confirm the existence of interlayer vibrational modes with ultralow frequencies ($<$40 cm^{-1}) in few-QL Bi_2Te_3 and Bi_2Se_3, as expected. In an NQL system, there are N-1 twofold degenerate interlayer shear modes (E_g) and N-1 nondegenerate interlayer breathing modes (A_{1g}) with different frequencies. Note that no interlayer vibrational modes exist in 1QL since there is no interlayer van der Waals restoring force, in good agreement with our experimental observations in 1QL Bi_2Se_3. The calculated phonon mode symmetries, Raman/IR activities, as well as

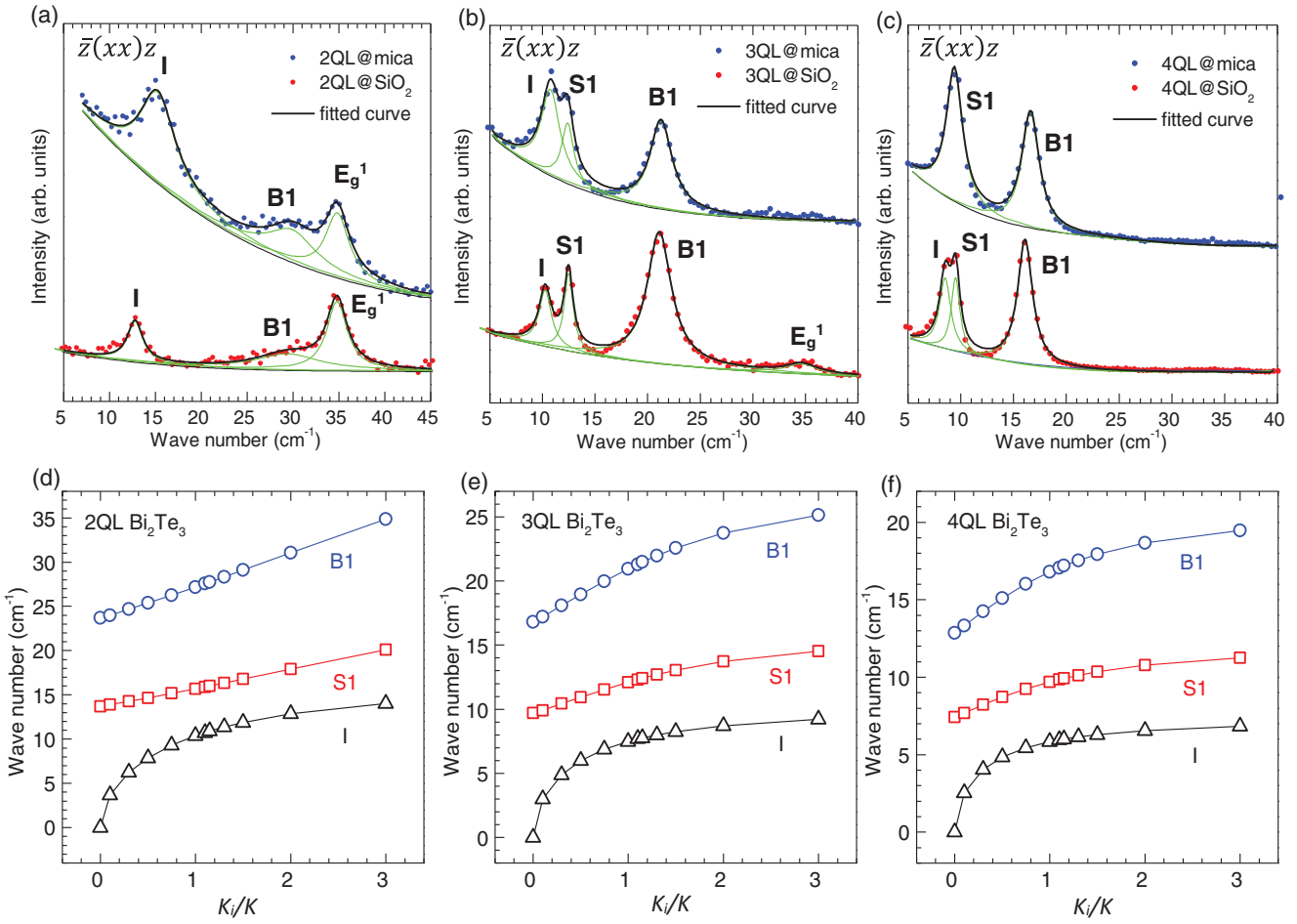

FIG. 5. (Color online) Substrate-dependent Raman spectra and force constant modeling of the I mode. (a) and (c) Low frequency Raman spectra of 2–4QL Bi_2Te_3 nanoplates grown on mica (blue dotted line) and SiO_2/Si substrates (red dotted line). The black solid lines are fitted results through the multi-Lorentzian fitting, and the green lines are the Lorentzian peaks involved. The frequencies of the S1 and B1 modes do not show a substrate dependence, while that of the I mode largely depends on the substrates. (d) and (f) Calculated frequencies of the B1, S1, and I modes of 2–4QL Bi_2Te_3 on a substrate with the ratio of the interface and interlayer force constants K_i/K varying from 0 to 3.

the relative Raman intensities under the $\bar{z}(xx)z$ polarization configuration are presented in Table S-III and Table S-IV (Supplemental Material [37]) for 2–5QL Bi_2Te_3 and Bi_2Se_3, respectively. In general, interlayer shear modes with the lowest, third lowest, or more generally the jth (j is odd number) lowest frequencies are Raman active (E_g), while the rest are IR active (E_u). Similarly, interlayer breathing modes with the jth (j is odd number) lowest frequencies are Raman active (A_{1g}), and the rest are IR active (A_{2u}). Nonresonant Raman intensity calculations within the Plazcek approximation [38,39] indicate that lowest frequency breathing (shear) modes carry the largest Raman intensities among all the Raman active interlayer breathing (shear) modes in any NQL, well explaining the experimental identification of the B1 and S1 modes in the Raman spectra (Fig. 3).

A comparison between the experimental data and DFT-calculated results are shown in Fig. 4. Figure 4(a) plots out the frequencies of the S1 (red solid squares) and B1 (blue solid circles) peaks in 2–8QL Bi_2Te_3 extracted from Fig. 3(a), as well as the calculated frequencies of the lowest frequency shear modes (red open squares) and the lowest frequency breathing modes (blue open circles) in 2–5QL Bi_2Te_3. Similarly, the frequencies of the S1 and B1 peaks extracted from Fig. 3(c) and the calculated results in 2–5QL Bi_2Se_3 are shown in Fig. 4(b). The experimental frequency evolution trends with varying thickness are well predicted by calculations for both the B1 and S1 modes. For 2–5QL Bi_2Te_3, the calculations overall underestimate the experimental values by an average of $\sim$4.8 cm^{-1} for the B1 mode and $\sim$2.9 cm^{-1} for the S1 mode; in 2–5QL Bi_2Se_3, the calculated results overestimate the experiments by an average of $\sim$1.2 cm^{-1} for the B1 mode and $\sim$1.5 cm^{-1} for the S1 mode. Beside the B1 and S1 modes, other experimentally observed minor low frequency peaks (mostly in 4QL and above), listed in Tables S-I and S-II (Supplemental Material [37]), might also correspond to some interlayer vibrational modes of higher frequencies, with vibration symmetries of either A_{1g} or E_g, depending on their polarization dependence in the Raman spectra. However, the exact normal mode assignment for these Raman peaks is not clear yet and is also beyond the scope of this paper.

The frequency evolutions of the S1 and B1 modes with varying thickness can be well understood by a simple linear

chain model with a substrate, whose schematic is shown in Fig. 4(d), with the blue spheres representing single QLs bonded by the van der Waals force with a force constant K. The interface interaction between the Bi_2X_3 thin films and the substrates is represented by a force constant K_i. This model further assumes that only interactions between the nearest-neighbor QLs are important. A similar model neglecting the substrate effect ($K_i = 0$) has previously been used to explain the interlayer vibrational modes in few-layer graphene [24] and transition metal dichalcogenides [21]. Solving the linear chain model assuming $K_i = 0$ Nm^{-3}, the frequencies (in cm^{-1}) of the eigenmodes can be obtained as

$$\omega_\alpha = \sqrt{\frac{K}{2\mu\pi^2c^2}\left(1-\cos\left(\frac{(\alpha-1)\pi}{N}\right)\right)}, \qquad (1)$$

where $\alpha = 1$ corresponds to the acoustic mode and $\alpha = 2,\ldots,N$ corresponds to the interlayer breathing modes ($K = K_z$) and shear modes ($K = K_x$). μ is the mass per unit area of one Bi_2X_3 QL ($\mu = 8.2\times10^{-6}$ kg/m^2 for Bi_2Te_3; $\mu = 7.5\times10^{-6}$ kg/m^2 for Bi_2Se_3), and c is the speed of light with the unit of centimeter per second. For the lowest frequency interlayer breathing (B1) and shear (S1) modes, the aforementioned expression with $\alpha = 2$ fits both the measured and computed results very well for both Bi_2Te_3 and Bi_2Se_3 (see the fitted solid and dashed lines in Figs. 4(a) and 4(b). The good fitting indicates that the interface interaction between Bi_2X_3 QLs and the substrates, if there is any, does not affect much the frequency evolutions of the interlayer vibrational modes with varying thickness. The in-plane and out-of-plane force constants for both Bi_2Te_3 and Bi_2Se_3 can be obtained from fitting the experimental and DFT calculated data, as shown in Table I. Overall, the DFT calculations underestimate the experimental force constants by a factor of ~1.7 for Bi_2Te_3 and overestimate that by a factor of ~1.3 for Bi_2Se_3. Both experiments and calculations suggest that the out-of-plane force constants (K_z) are larger than the in-plane ones (K_x), by a factor of ~2.9 for Bi_2Te_3 and ~2.2 for Bi_2Se_3, similar to other layered materials, such as MoS_2 and WSe_2, where K_z has been reported to be about three times as large as K_x [21].

Figure 4(e) shows the vibration schematics of the lowest frequency shear mode (S1) and lowest frequency breathing mode (B1) in 2QL, where the vibration directions are guided by the arrows with lengths proportional to the displacement magnitudes. The schematics of all the interlayer vibrational modes in 2–5QL are shown in Figure S-2 (Supplemental Material [37]). In any NQL system, the S1 and B1 modes have a similar vibration manner: the QLs are divided into two groups, which are vibrating out-of-phase, while the QLs within each group are vibrating in-phase. This picture is consistent with the S1 (B1) mode having the lowest frequency among its suit of phonon modes without considering the zero frequency acoustic mode, because more out-of-phase vibrations between QLs will result in higher frequencies (see Figure S-2 and Tables S-III and S-IV of the Supplemental Material [37]). In the frame of the linear chain model, the S1 (B1) mode can be viewed as a half transverse (longitudinal) standing wave supported along the chain length with the top and bottom QLs being the wave crest and valley, respectively, corresponding to the eigenmode with the lowest frequency.

TABLE I. Force constants per unit area derived from fits to the linear chain model in few-QL Bi_2Te_3 and Bi_2Se_3.

		DFT (LDA)	Experiment
Bi_2Te_3	$K_z(10^{19}$ Nm$^{-3})$	8.21	13.33
	$K_x(10^{19}$ Nm$^{-3})$	2.76	4.57
Bi_2Se_3	$K_z(10^{19}$ Nm$^{-3})$	6.34	5.26
	$K_x(10^{19}$ Nm$^{-3})$	3.10	2.27

Besides the lowest frequency breathing (B1) and shear (S1) modes, a Raman peak with even lower frequency has been identified in 2–4QL Bi_2Te_3. Due to the low frequency of this mode, it is likely that this mode results from the weak interface interactions between Bi_2Te_3 nanoplates and the substrates, and we tentatively call it an interface mode (I). To investigate this hypothesis, we conduct substrate-dependent Raman studies. Figures 5(a)–5(c) show the low frequency Raman spectra of 2–4QL Bi_2Te_3 on SiO_2/Si and mica substrates, respectively. The spectra are carefully analyzed through multi-Lorentzian fitting on top of a polynomial background. While the B1 and S1 peaks barely show any substrate dependence, the I peak is very sensitive to the substrate, which supports its origin of a substrate introduced I mode. Also, note that the full-range Raman spectra are essentially the same for Bi_2Te_3 2D crystals on SiO_2/Si and mica substrates, except for the different I peaks in 2–4QL. In 2–3QL, a higher frequency of the I peak is found on the mica substrates than on SiO_2/Si. In 4QL, the I peak is very close to the S1 peak on SiO_2/Si but can barely be distinguished on mica. The high sensitivity of the I mode to choices of substrates indicates different interaction strengths at different sample-substrate interfaces.

We model the effects of the interaction between Bi_2Te_3 nanoplates and the substrates by using a nonzero substrate-introduced force (force constant K_i) in the linear chain model with a substrate as described above [Fig. 4(d)]. This nonzero K_i results in eigenmodes that are different from those of the free linear chain model ($K_i = 0$). Most distinctly, the zero-frequency acoustic mode corresponding to the eigenmode with $\alpha = 1$ becomes an I mode with finite frequency due to the presence of a restoring force. In order to understand how the interface force constants affect the observed frequencies, we fix the interlayer force constants to those derived for the free linear chain model fitting of the DFT-calculated data (see Table I) and vary the ratio between K_i and the interlayer force constant K. As shown in Figs. 5(d)–5(f), for all values of K_i/K from 0 to 3, the frequency of the I mode is smaller than the S1 and B1 frequencies in 2–4QL Bi_2Te_3. Furthermore, for $K_i/K < 1$, the frequency of the I mode exhibits significantly stronger dependence on the value of K_i/K compared to the interlayer modes S1 and B1. Therefore, the experimental observations of the low frequency peak I in few-QL Bi_2Te_3 is consistent with the presence of an interaction between Bi_2Te_3 and the substrates. Moreover, the strong dependence of the I peak frequency on the choice of substrates [Figs. 5(a)–5(c)] indicates that the substrate-induced interaction is likely to be weaker than the interlayer interaction within the as-grown Bi_2Te_3 nanoplates, while it is still significant to give rise to the I mode. In the as-grown few-QL Bi_2Se_3 nanoplates

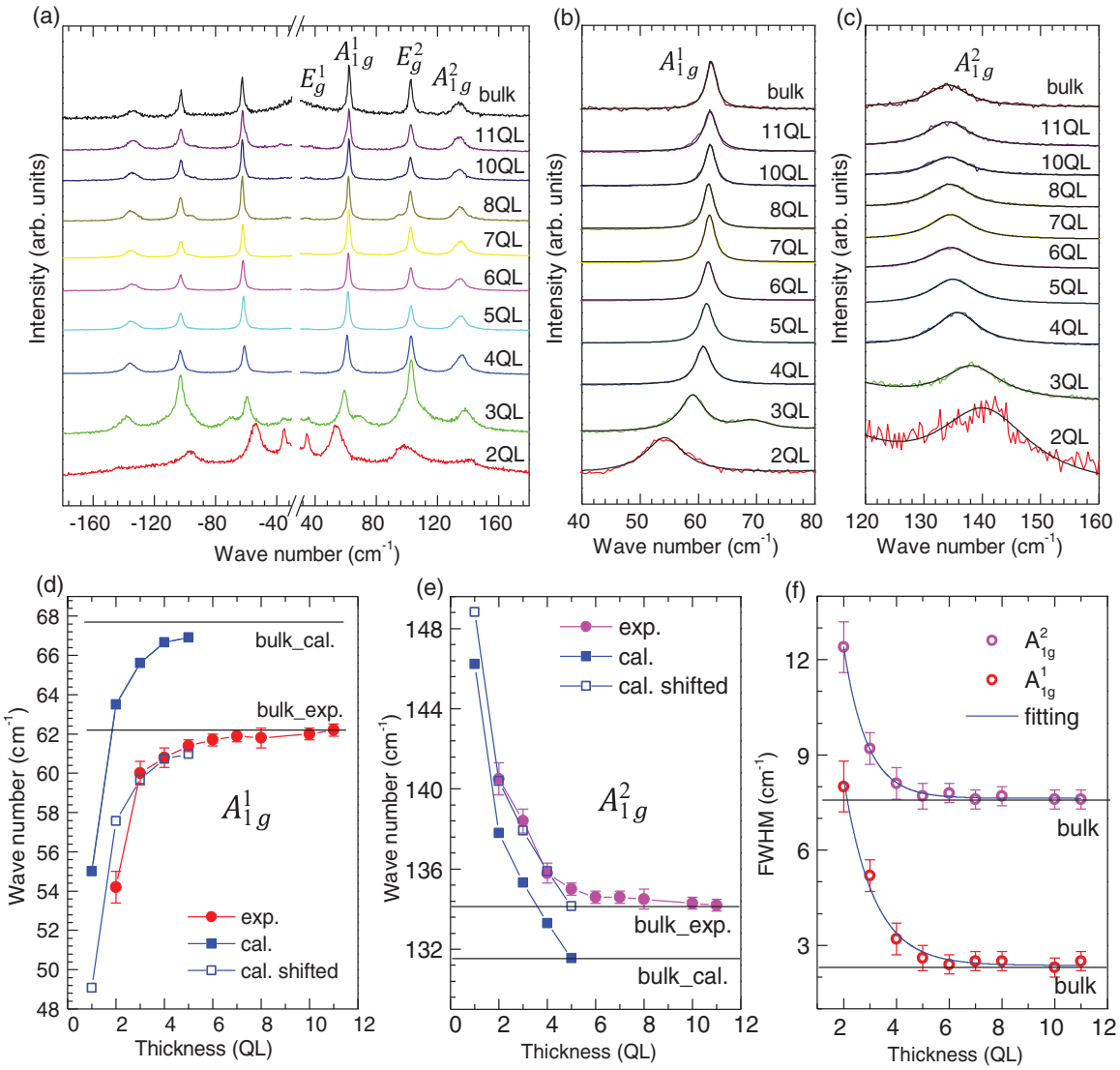

FIG. 6. (Color online) Raman spectra of few-QL Bi_2Te_3 and analysis. (a) High frequency Stokes and anti-Stokes Raman spectra of bulk Bi_2Te_3 and 2–11QL nanoplates on SiO_2/Si substrates. (b) and (c) Zoom-in view of the (b) A^1_{1g} and (c) A^2_{1g} peaks with varying thicknesses. (d) A^1_{1g} mode frequency versus nanoplate thickness. The red solid circles are experimental data and the blue solid squares are the calculated results. The calculated data are downshifted by 5.9 cm^{-1} (blue open squares) to match the experimental bulk frequency. (e) A^2_{1g} mode frequency versus nanoplate thickness. The pink solid circles are experimental data, and the blue solid squares are the calculated results. The calculated data are upshifted by 2.6 cm^{-1} (blue open squares) to match the experimental bulk frequency. (f) FWHM versus thickness of both A^1_{1g} and A^2_{1g} modes and the phenomenological fittings.

on mica, as well as the mechanically exfoliated multilayer graphene, MoS_2 and WSe_2 on SiO_2/Si, the substrate-induced interaction is likely to be negligible since the low frequency mode I has not yet been observed [21,24]. The origin of this larger substrate-induced interaction for Bi_2Te_3 is unclear and requires further investigations. As an illustration, we plot the eigenmode frequencies calculated from the linear chain model with a substrate with $K_i/K = 0.5$ in Fig. 4(c). The displacement schematics of the I mode and interlayer B1 and S1 modes in 2QL Bi_2Te_3 on a substrate are displayed in Fig. 4(f). Compared to the free linear chain model [Fig. 4(e)], the substrate plays its role by slightly changing the relative displacement magnitudes of the QLs, while keeping the overall vibration patterns, which consequently causes the change of phonon mode frequencies. Note that, in principle, the interface mode exists in all the as-grown Bi_2Te_3 2D crystals. Experimentally, we did not identify this mode above 4QL because it is either overwhelmed by the strong S1 peak or falls in the frequency regime beyond our detection limit.

We next discuss the high frequency phonon behavior from 3D to 2D Bi_2X_3. Figure 6(a) shows the Stokes and anti-Stokes Raman spectra in the high frequency region (30–160 cm^{-1}) measured from 2–11QL and bulk Bi_2Te_3. Four intrinsic Raman active modes of bulk are observed around 36 cm^{-1} (E^1_g), 62 cm^{-1} (A^1_{1g}), 102 cm^{-1} (E^2_g), 133 cm^{-1} (A^2_{1g}) in bulk and few-QLs. Note that the E^1_g peak is very weak but is much pronounced when the thickness is decreased to 2QL, in contrast to the distinct E^1_g peak in the Bi_2Te_3 thin films grown by

molecular beam epitaxy (MBE) [16]. From bulk to 2QL, the A_{1g}^1 exhibits a redshift of $\sim 8\,\mathrm{cm}^{-1}$, while the A_{1g}^2 peak blueshifts by $\sim 6\,\mathrm{cm}^{-1}$. In comparison, the E_g^2 peak barely shows any frequency shift from 3D to 2D. It is worth noting that in general, the out-of-plane modes have higher sensitivity to the nanoplate thickness than the in-plane modes, consistent with our observations in the low frequency region, as well as previous reports [15,16]. A careful lineshape analysis was conducted for the Raman spectra and good Lorentzian fitting was achieved [Figs. 6(b) and 6(c)]; the fitted frequencies and full widths at half-maximum (FWHMs) of the A_{1g}^1 and A_{1g}^2 peaks are plotted as a function of QL number [Figs. 6(d)–6(f)]. Besides the frequency shifts, the FWHMs of both A_{1g}^1 and A_{1g}^2 peaks increase with decreasing thickness, especially in the 2D limit. In few-QL Bi_2Se_3, there exist very similar Raman peak shifts and broadening with decreasing thickness, consistent with our previous Raman studies in the same system [15], and, therefore, will not be discussed in detail here.

The frequency evolution of the A_{1g}^1 and A_{1g}^2 peaks from 3D to 2D Bi_2Te_3 origins from the phonon confinement effect [40] and can be numerically predicted by DFT calculations. The calculated frequencies of the A_{1g}^1 and A_{1g}^2 modes in 2–5QL Bi_2Te_3 are shown in Figs. 6(d) and 6(e) as blue solid squares, and the experimental results are presented by the red and pink solid spheres. Overall, the calculations overestimate the experimental frequency of the A_{1g}^1 mode and underestimate that of the A_{1g}^2 mode. In the bulk, the discrepancies are 5.9 and $2.6\,\mathrm{cm}^{-1}$, respectively, still within the systematic error bar [41]. The calculated frequency evolution trends, however, agree with the experiments well. A clearer demonstration can be made by systematically shifting the calculated data to achieve perfect agreement between the experiments and calculations in the bulk limit, as shown by the blue open squares in Figs. 6(d) and 6(e). The broadening of the A_{1g}^1 and A_{1g}^2 peaks with decreasing thickness follows the phenomenological exponential relationship $\Gamma_0(d) = A + B\exp(-d/C)$, where d represents the thickness of the Bi_2Te_3 nanoplates, and A, B, and C are fitting parameters [15,42]. Good fitting was achieved with $A = 2.4 \pm 0.08$, $B = 33.9 \pm 7.9$, and $C = 1.1 \pm 0.1$ for A_{1g}^1 and $A = 7.6 \pm 0.03$, $B = 46.0 \pm 7.4$, and $C = 0.9 \pm 0.05$ for A_{1g}^2, as shown by the blue solid lines in Fig. 6(f). The broadening of a Raman peak corresponds to a decreased phonon lifetime, and this phonon confinement effect becomes more dominant when the sample size is closer to the extreme 2D limit.

IV. CONCLUSIONS

In summary, the phonon properties in bulk and 2D Bi_2Te_3 and Bi_2Se_3 have been systematically investigated, through the combination of Raman spectroscopy, first-principles calculations, and group theory analysis. Crystal dimensionality plays a key role in determining the quantity and vibration symmetry of the phonon modes. The low frequency interlayer breathing and shear modes that have been uncovered in the Bi_2X_3 2D crystals are, however, excluded in the 3D bulk due to the symmetry change. The frequency evolution of the interlayer vibrational modes with varying crystal thickness can be well interpreted by a linear chain model, which functions as an effective probe of the interlayer van der Waals force. An ultralow frequency interface mode has been identified in 2D Bi_2Te_3, which we tentatively propose to originate from the substrate-crystal interface interactions. The thickness dependence of the high frequency Raman spectra reveals the phonon confinement effect in the 2D limit, which can also be well predicted by the DFT calculations. Our results brought to light a full picture of the phonon properties and their dependency on the crystal symmetry and dimensionality in the layered bismuth chalcogenide topological insulator materials.

ACKNOWLEDGMENTS

Q.X. gratefully acknowledges the strong support of this paper from the Singapore National Research Foundation (NRF) through a fellowship (Grant No. NRF-RF2009-06). This work was also supported, in part, by the Ministry of Education (Singapore) via Tier 2 (Grant No. MOE2012-T2-2-086), start-up support (Grant No. M58113004), and New Initiative Fund (Grant No. M58110100) from Nanyang Technological University (NTU). S.Y.Q and X.L gratefully acknowledge the Agency for Science, Technology, and Research (A*STAR) for funding under the Institute of High Performance Computing Independent Investigatorship and the Singapore NRF for funding under the NRF Fellowship (NRF-NRFF2013-07). The computations were performed at the National University of Singapore Graphene Research Centre cluster and the A*STAR Computational Resource Center, with support from the Institute of High Performance Computing.

[1] K. J. Koski and Y. Cui, ACS Nano **7**, 3739 (2013).
[2] S. Z. Butler, S. M. Hollen, L. Cao, Y. Cui, J. A. Gupta, H. R. Gutiérrez, T. F. Heinz, S. S. Hong, J. Huang, A. F. Ismach, E. Johnston-Halperin, M. Kuno, V. V. Plashnitsa, R. D. Robinson, R. S. Ruoff, S. Salahuddin, J. Shan, L. Shi, M. G. Spencer, M. Terrones *et al.*, ACS Nano **7**, 2898 (2013).
[3] G. S. Nolas, J. Sharp, and H. J. Goldsmid, *Thermoelectrics: Basic Principles and New Materials Developments* (Springer, New York, 2001).
[4] H. Zhang, C.-X. Liu, X.-L. Qi, X. Dai, Z. Fang, and S.-C. Zhang, Nat. Phys. **5**, 438 (2009).
[5] H. Peng, K. Lai, D. Kong, S. Meister, Y. Chen, X.-L. Qi, S.-C. Zhang, Z.-X. Shen, and Y. Cui, Nat. Mater. **9**, 225 (2010).
[6] F. Xiu, L. He, Y. Wang, L. Cheng, L.-T. Chang, M. Lang, G. Huang, X. Kou, Y. Zhou, and X. Jiang, Nat. Nanotechnol. **6**, 216 (2011).
[7] A. A. Taskin, S. Sasaki, K. Segawa, and Y. Ando, Phys. Rev. Lett. **109**, 066803 (2012).
[8] D. Kong, Y. Chen, J. J. Cha, Q. Zhang, J. G. Analytis, K. Lai, Z. Liu, S. S. Hong, K. J. Koski, S.-K. Mo, Z. Hussain, I. R. Fisher, Z.-X. Shen, and Y. Cui, Nat. Nanotechnol. **6**, 705 (2011).

[9] Y. Min, J. W. Roh, H. Yang, M. Park, S. I. Kim, S. Hwang, S. M. Lee, K. H. Lee, and U. Jeong, Adv. Mater. **25**, 1425 (2013).
[10] A. Soni, Z. Yanyuan, Y. Ligen, M. K. K. Aik, M. S. Dresselhaus, and Q. Xiong, Nano Lett. **12**, 1203 (2012).
[11] J. S. Son, M. K. Choi, M.-K. Han, K. Park, J.-Y. Kim, S. J. Lim, M. Oh, Y. Kuk, C. Park, and S.-J. Kim, Nano Lett. **12**, 640 (2012).
[12] A. Soni, Y. Shen, M. Yin, Y. Zhao, L. Yu, X. Hu, Z. Dong, K. A. Khor, M. S. Dresselhaus, and Q. Xiong, Nano Lett. **12**, 4305 (2012).
[13] X. Luo, M. B. Sullivan, and S. Y. Quek, Phys. Rev. B **86**, 184111 (2012).
[14] W. Cheng and S.-F. Ren, Phys. Rev. B **83**, 094301 (2011).
[15] J. Zhang, Z. Peng, A. Soni, Y. Zhao, Y. Xiong, B. Peng, J. Wang, M. S. Dresselhaus, and Q. Xiong, Nano Lett. **11**, 2407 (2011).
[16] C. Wang, X. Zhu, L. Nilsson, J. Wen, G. Wang, X. Shan, Q. Zhang, S. Zhang, J. Jia, and Q. Xue, Nano Res. **6**, 688 (2013).
[17] R. He, Z. Wang, R. L. J. Qiu, C. Delaney, B. Beck, T. E. Kidd, C. C. Chancey, and X. P. A. Gao, Nanotechnology **23**, 455703 (2012).
[18] W. Dang, H. Peng, H. Li, P. Wang, and Z. Liu, Nano Lett. **10**, 2870 (2010).
[19] K. M. F. Shahil, M. Z. Hossain, D. Teweldebrhan, and A. A. Balandin, Appl. Phys. Lett. **96**, 153103 (2010).
[20] X. Luo, Y. Zhao, J. Zhang, M. Toh, C. Kloc, Q. Xiong, and S. Y. Quek, Phys. Rev. B **88**, 195313 (2013).
[21] Y. Zhao, X. Luo, H. Li, J. Zhang, P. T. Araujo, C. K. Gan, J. Wu, H. Zhang, S. Y. Quek, M. S. Dresselhaus, and Q. Xiong, Nano Lett. **13**, 1007 (2013).
[22] C. H. Lui and T. F. Heinz, Phys. Rev. B **87**, 121404 (2013).
[23] X. Zhang, W. P. Han, J. B. Wu, S. Milana, Y. Lu, Q. Q. Li, A. C. Ferrari, and P. H. Tan, Phys. Rev. B **87**, 115413 (2013).
[24] P. H. Tan, W. P. Han, W. J. Zhao, Z. H. Wu, K. Chang, H. Wang, Y. F. Wang, N. Bonini, N. Marzari, N. Pugno, G. Savini, A. Lombardo, and A. C. Ferrari, Nat. Mater. **11**, 294 (2012).
[25] Y. Zhao, M. de la Mata, R. L. J. Qiu, J. Zhang, X. Wen, C. Magen, X. P. A. Gao, J. Arbiol, and Q. Xiong, Nano Res. **7**, 1243 (2014).
[26] H. Li, J. Cao, W. Zheng, Y. Chen, D. Wu, W. Dang, K. Wang, H. Peng, and Z. Liu, J. Am. Chem. Soc. **134**, 6132 (2012).
[27] P. Giannozzi, S. Baroni, N. Bonini, M. Calandra, R. Car, C. Cavazzoni, D. Ceresoli, G. Chiarotti, M. Cococcioni, I. Dabo, A. Corso, S. de Gironcoli, S. Fabris, G. Fratesi, R. Gebauer, U. Gerstmann, C. Gougoussis, A. Kokalj, M. Lazzeri, L. Martin-Samos *et al.*, J. Phys.: Condens. Matter **21**, 395502 (2009).
[28] J. P. Perdew and A. Zunger, Phys. Rev. B **23**, 5048 (1981).
[29] D. R. Hamann, Phys. Rev. B **40**, 2980 (1989).
[30] J. O. Jenkins, J. A. Rayne, and R. W. Ure, Jr., Phys. Rev. B **5**, 3171 (1972).
[31] V. Wagner, G. Dolling, B. M. Powell, and G. Landweher, Phys. Status Solidi B **85**, 311 (1978).
[32] W. Richter and C. R. Becker, Phys. Status Solidi B **84**, 619 (1977).
[33] T. C. Damen, S. P. S. Porto, and B. Tell, Phys. Rev. **142**, 570 (1966).
[34] W. Liu, X. Peng, X. Wei, H. Yang, G. M. Stocks, and J. Zhong, Phys. Rev. B **87**, 205315 (2013).
[35] S. Urazhdin, D. Bilc, S. D. Mahanti, S. H. Tessmer, T. Kyratsi, and M. G. Kanatzidis, Phys. Rev. B **69**, 085313 (2004).
[36] W. Kullmann, J. Geurts, W. Richter, N. Lehner, H. Rauh, U. Steigenberger, G. Eichhorn, and R. Geick, Phys. Status Solidi B **125**, 131 (1984).
[37] See Supplemental Material at http://link.aps.org/supplemental/10.1103/PhysRevB.90.245428 for the calculated frequencies and normal mode displacements for all the interlayer vibrations.
[38] P. Bruesch, *Phonons: Theory and Experiments II* (Springer, Berlin, 1986), Vol. 2.
[39] M. Lazzeri and F. Mauri, Phys. Rev. Lett. **90**, 036401 (2003).
[40] H. Richter, Z. P. Wang, and L. Ley, Solid State Commun. **39**, 625 (1981).
[41] X. Luo, Y. Zhao, J. Zhang, Q. Xiong, and S. Y. Quek, Phys. Rev. B **88**, 075320 (2013).
[42] S. L. Zhang, S. N. Wu, Y. Yan, T. Hu, J. Zhao, Y. Song, Q. Qu, and W. Ding, J. Raman Spectrosc. **39**, 1578 (2008).